Classification and materials realization of topologically robust nodal ring phonons

R. Y. Wang,[1] Z. J. Chen,[1,2] Z. Q. Huang,[1] B. W. Xia,[1] and H. Xu[1,3,4,*]

[1]*Department of Physics & Institute for Quantum Science and Engineering, Southern University of Science and Technology, Shenzhen 518055, People's Republic of China*

[2]*Department of Physics, South China University of Technology, Guangzhou 510640, People's Republic of China*

[3]*Guangdong Provincial Key Laboratory of Computational Science and Material Design, Southern University of Science and Technology, Shenzhen 518055, People's Republic of China*

[4]*Shenzhen Key Laboratory for Advanced Quantum Functional Materials and Devices, Southern University of Science and Technology, Shenzhen 518055, People's Republic of China*

(Received 22 February 2021; revised 1 July 2021; accepted 28 July 2021; published 12 August 2021)

Nodal ring phonons with topologically nontrivial properties have triggered much interest in recent years. Unlike fermions inevitably affected by the spin-orbit interaction, nodal ring phonons are topologically robust. In this paper, we investigate the classification of nodal rings in phonon systems based on symmetry arguments and $\boldsymbol{k}\cdot\boldsymbol{p}$ models. We identify that all the nodal ring phonons can be categorized into three types, i.e., in-plane nodal rings protected by mirror symmetry, twisted nodal rings protected by inversion and time-reversal symmetries, and the hybrid type protected by a combination of these symmetries. On the basis of first-principles calculations, we propose that these three types of nodal ring phonons can emerge in two different phases of silver oxide. The calculation results also show clear drumheadlike surface states along high-symmetry paths and nontrivial arc states in the isofrequency surfaces. This work exposes various appearances of nodal rings and also promotes the development of topological phonons.

DOI: 10.1103/PhysRevMaterials.5.084202

I. INTRODUCTION

Topological semimetals [1–3] greatly expand our understanding of condensed-matter physics and have become one of the most active topics in recent years. In topological semimetals, fascinating degenerate manifolds of different dimensions stem from the crossings of conduction and valence bands, forming zero-dimensional Dirac/Weyl points [4–8] or one-dimensional nodal lines [9,10] near the Fermi level. Among these topological phases, Dirac/Weyl points are well known due to their corresponding particles, i.e., Dirac/Weyl fermions, in high-energy physics. By contrast, nodal lines have attracted great attention as the crystal symmetry endows them with various appearances that are robust against random perturbations. As an indispensable part of nodal lines, nodal rings featured by enclosed curves in momentum space are of great interest. So far, intense efforts have been devoted to discovering new types of nodal rings depending on their shapes, e.g., the most common single nodal rings, crossed nodal rings [11–13], nodal chains [14,15], and Hopf links [16–18], which immensely enrich our knowledge of topological physics.

In electronic systems, nodal rings are vulnerable in realistic materials since the spin-orbit coupling (SOC) effect must be taken into account, usually turning nodal ring semimetals into ordinary insulators, topological insulators, or Weyl semimetals [19,20]. In comparison, nodal ring phonons are topologically robust in realistic materials [21–23]. On the one hand, the SOC effect is ignorable since the SU(2) symmetry is preserved for spinless phonons [24]. On the other hand, phonons do not respect the Pauli exclusion principle, so that nodal ring phonons can emerge in any range of frequency. Moreover, many quantum concepts such as topology, Berry phase, and pseudospin have been introduced into phonon systems, which is beneficial for potential applications in phonon waveguides, thermoelectrics, thermal isolation, and other devices related to the thermal Hall effect and the light response [25–27]. To date, nodal ring phonons have been put forward in several realistic materials, for example, intersecting nodal ring phonons in C_8 with a body-centered cubic structure [28] and ideal type-III nodal ring phonons in $CaMg_2$ [29]. However, the classification of nodal ring phonons and the corresponding materials are still lacking.

In this paper, nodal ring phonons in crystalline solids are comprehensively investigated. Based on symmetry protection mechanisms, we divide all systems with nodal ring phonons into three types, as shown in Fig. 1. In the first case [see Fig. 1(a)], the nodal rings are protected by mirror symmetries, and thus are completely constrained in the mirror planes. In the second type [see Fig. 1(b)], the nodal ring is protected by inversion and time-reversal symmetries, which is distributed twistingly and centrosymmetrically about the time-reversal invariant momenta. The third type [see Fig. 1(c)], protected by a combination of mirror, inversion, and time-reversal symmetries, is termed a hybrid nodal ring, resulting in some intersections at high-symmetry momenta. By using first-principles calculations, we perform high-throughput screening to search for materials with

*xuh@sustech.edu.cn

 ©2021 American Physical Society

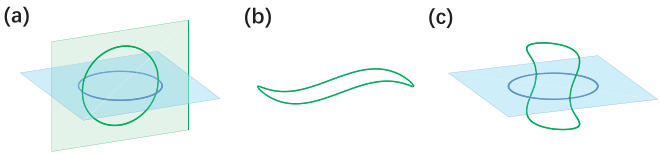

FIG. 1. (a) Nodal rings protected by mirror symmetries. (b) A nodal ring protected by inversion and time-reversal symmetries. (c) Hybrid nodal rings protected by mirror, inversion, and time-reversal symmetries.

topological nodal ring phonons. In the main text, we take two different phases of AgO [30,31] as examples, and more candidate materials are given in the Supplemental Material [32].

II. COMPUTATIONAL METHODS

We use the Vienna *ab initio* simulation package (VASP) [35] to perform first-principles calculations based on density functional theory [36], and the cutoff energy is taken as 520 eV. The exchange-correlation energy is described by the generalized gradient approximation (GGA) in the form of the Perdew-Burke-Ernzerhof (PBE) function [37], and the core-valence interactions are dealt with the projector augmented-wave (PAW) method [38,39]. The phonon dispersions are attained by diagonalization of real-space force constants as implemented in the PHONOPY package [40]. The phonon Hamiltonian of the tight-binding (TB) model is obtained with the WANNIERTOOLS package [41].

III. CLASSIFICATION AND MATERIALS REALIZATION

A. Nodal rings protected by mirror symmetries

To reveal the nontrivial topology of mirror-protected nodal ring phonons, we use a $2 \times 2\, \boldsymbol{k} \cdot \boldsymbol{p}$ Hamiltonian to describe the dispersion of two phonon branches,

$$\mathcal{H}(\boldsymbol{q}) = d_0(\boldsymbol{q})\sigma_0 + \sum_{i=x,y,z} d_i(\boldsymbol{q})\sigma_i, \tag{1}$$

where σ_i are three Pauli matrices [$\sigma_x = \left(\begin{smallmatrix} 0 & 1 \\ 1 & 0 \end{smallmatrix}\right)$, $\sigma_y = \left(\begin{smallmatrix} 0 & -i \\ i & 0 \end{smallmatrix}\right)$, $\sigma_z = \left(\begin{smallmatrix} 1 & 0 \\ 0 & -1 \end{smallmatrix}\right)$], σ_0 is a 2×2 identity matrix, $d_i(\boldsymbol{q})$ are real functions about momentum $\boldsymbol{q} = (q_x, q_y, q_z)$, and $d_0(\boldsymbol{q})$ is the kinetic term, which will be omitted hereafter since $d_0(\boldsymbol{q})\sigma_0$ simply moves the energy position of the band crossings without affecting the degeneracy and dispersion. Considering a high-symmetry plane with M_z symmetry, the invariant theory demands

$$M_z \mathcal{H}(q_x, q_y, q_z) M_z^{-1} = \mathcal{H}(q_x, q_y, -q_z). \tag{2}$$

Equation (2) indicates that the Hamiltonian $\mathcal{H}(\boldsymbol{q})$ and M_z are commutative when $q_z = 0$, so that the phonon branches can be labeled by the eigenvalues of M_z, which are ± 1 since $M_z^2 = 1$. Two branches with different eigenvalues might cross each other, forming a complete ring in the mirror plane.

As mentioned above, the matrix representation of the M_z symmetry can be chosen as σ_z according to its eigenvalues. Substituting M_z with σ_z, Eq. (2) indicates that $d_{x,y}(\boldsymbol{q})$ are odd functions and $d_z(\boldsymbol{q})$ is an even function about q_z. The appearance of band crossings requires $q_z = 0$ because it is the sole common solution of $d_{x,y}(\boldsymbol{q}) = 0$. Then the last term $d_z(\boldsymbol{q})$ can be expanded as

$$d_z(\boldsymbol{q}) = \sum_{i=x,y,z} C_z^{ii} q_i^2 + \sum_{i=x,y} C_z^i q_i + C_z^{xy} q_x q_y + C_z + O_z^2(\boldsymbol{q}), \tag{3}$$

where $O_z^2(\boldsymbol{q})$ means the terms with an order greater than 2. A complete ring will emerge under appropriate parameters, for example, when the solution of $d_z(\boldsymbol{q}) = 0$ generates an enclosed three-dimensional manifold such as an ellipsoid ($C_z C_z^{ii} < 0$). It is worth noting that more than one mirror will probably engender crossed mirror-protected nodal rings due to the various combinations of mirrors in crystals.

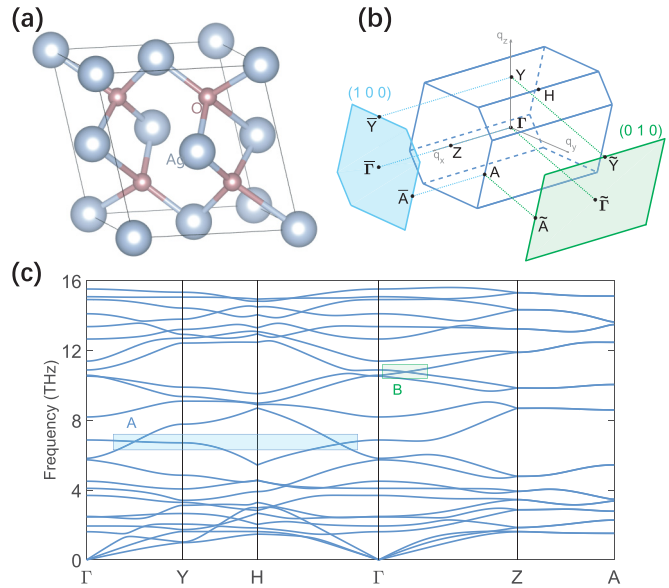

FIG. 2. (a) Crystal structure of AgO with space group $P2_1/c$. (b) Bulk Brillouin zone and projected Brillouin zone of the (100) and (010) surfaces. (c) Calculated phonon spectrum of AgO.

The above arguments can be confirmed in the monoclinic AgO with space group $P2_1/c$ (No. 14), which possesses a mirror symmetry to ensure the emergence of nodal ring phonons. In addition, an inversion symmetry and a C_2 rotational symmetry coexist in space group $P2_1/c$. The primitive cell and the first Brillouin zone are shown in Figs. 2(a) and 2(b), respectively. The optimized lattice constants are $a = 5.635$ Å, $b = 3.776$ Å, and $c = 5.575$ Å, which are consistent with previous work [30]. The four silver atoms in the primitive cell occupy $2a$ (0, 0, 0) and $2d$ (0.5, 0, 0.5), and four oxygen atoms occupy the $4e$ (0.289, 0.815, 0.275) Wyckoff positions. Figure 2(c) shows the phonon spectrum of AgO along the high-symmetry paths, and it is conspicuous that the crossings appear along the H-Γ-Y (area A) and Γ-Z (area B) directions. The crossing points in area A [see Fig. 3(a) in detail] come from a topological nodal ring totally constrained in a plane shown in Fig. 3(b), which turns out to be protected by mirror symmetry. The only subtle difference from the above derivation is that the mirror is on the $q_x = 0$ plane instead of $q_z = 0$. Besides, the crossing point in area B [see also Fig. 4(a)] will be analyzed in the next section.

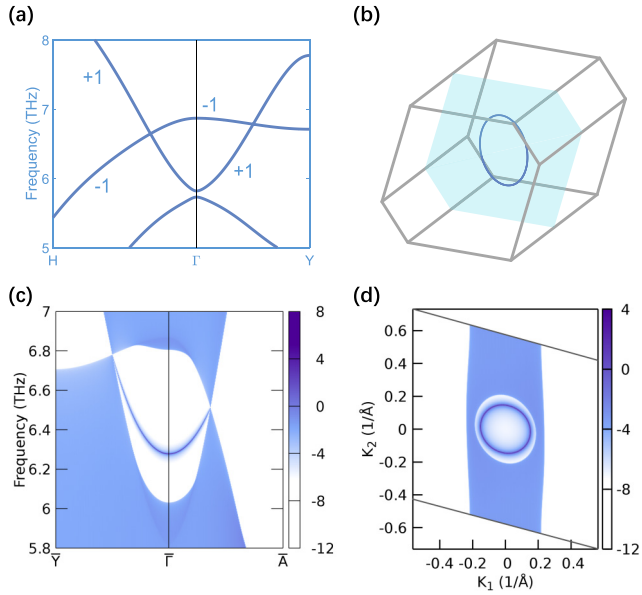

FIG. 3. (a) Phonon spectrum along the H-Γ-Y direction. (b) Nodal ring protected by M_x mirror symmetry. (c) Phonon surface states along the $\bar{Y}$-$\bar{\Gamma}$-$\bar{A}$ direction of the (100) surface. (d) Phonon surface arcs on the (100) surface Brillouin zone. The units of color bars in (c) and (d) are in arbitrary units.

To confirm the topological properties, we calculate the Berry phases $\gamma = \oint_C \mathcal{A}(\boldsymbol{q}) \cdot d\boldsymbol{q}$ of all the candidate materials, where $\mathcal{A}(q)$ is the Berry connection $-i\sum_j \langle\varphi_j(\boldsymbol{q})|\nabla_{\boldsymbol{q}}|\varphi_j(\boldsymbol{q})\rangle$, $\varphi_j(\boldsymbol{q})$ is the Bloch wave function of the jth phonon branch, and C is a path that encircles the nodal ring. The calculated results are π, showing the nontrivial topology of nodal ring phonons. We also show the local phonon density of states on the (100) surface ranging from 5.8 to 7.0 THz in Fig. 3(c). Two bulk linear crossings are observed along the $\bar{Y}$-$\bar{\Gamma}$-$\bar{A}$ direction, and the drumheadlike surface states clearly appear between these two linear crossings. In Fig. 3(d), we further provide the isofrequency surface at 6.4 THz, in which there are visible and almost circular arc states that match with the nontrivial surface states in Figs. 3(a) and 3(c). Such topological surface states are clearly visible, indicating the possibility to be observed in experiments.

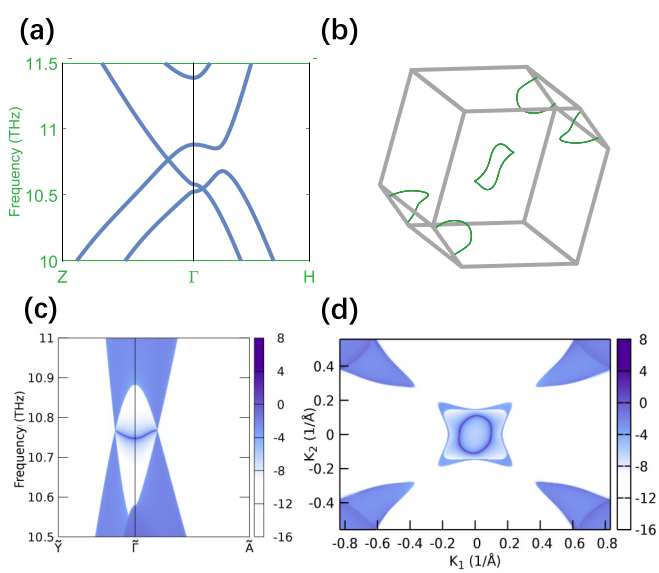

FIG. 4. (a) Phonon spectrum along the Z-Γ-H direction. (b) Nodal rings protected by inversion and time-reversal symmetries. (c) Phonon surface states along the $\tilde{Y}$-$\tilde{\Gamma}$-$\tilde{A}$ direction of the (010) surface. (d) Phonon surface arcs on the (010) surface Brillouin zone. The units of color bars in (c) and (d) are in arbitrary units.

B. Nodal rings protected by inversion and time-reversal symmetries

An additional condition for the existence of stable nodal rings protected by inversion and time-reversal symmetries is the presence of SU(2) symmetry. That is to say, this type of nodal rings cannot emerge in electronic systems. Using the $\boldsymbol{k}\cdot\boldsymbol{p}$ Hamiltonian, we expound its formation in detail. In a phononic system with time-reversal symmetry, we know

$$\mathcal{T}\mathcal{H}(\boldsymbol{q})\mathcal{T}^{-1} = \mathcal{H}(-\boldsymbol{q}). \tag{4}$$

The time-reversal symmetry $\mathcal{T}$ can be represented by a complex conjugate operator $\mathcal{K}$ in phononic systems, and then we can conclude that $d_{x,z}(\boldsymbol{q})$ are even functions with regard to $\boldsymbol{q}$ and $d_y(\boldsymbol{q})$ is an odd function. Besides, the inversion operator can be represented by σ_z if the eigenvalues of the inversion symmetry for two crossing branches are ± 1, namely

$$\mathcal{P}\mathcal{H}(\boldsymbol{q})\mathcal{P}^{-1} = \mathcal{H}(-\boldsymbol{q}), \tag{5}$$

which gives that $d_{x,y}(\boldsymbol{q})$ are odd functions and $d_z(\boldsymbol{q})$ is an even function. As a result, Eqs. (4) and (5) give $d_x(\boldsymbol{q}) = 0$, $d_y(\boldsymbol{q}) = -d_y(-\boldsymbol{q})$, and $d_z(\boldsymbol{q}) = d_z(-\boldsymbol{q})$. Therefore, with the constraints of these two symmetries, $d_i(\boldsymbol{q})$ can be written as

$$d_y(\boldsymbol{q}) = \sum_{i=x,y,z} C_y^i q_i + O_y^1(\boldsymbol{q}),$$
$$d_z(\boldsymbol{q}) = \sum_{i,j=x,y,z} C_z^{ij} q_i q_j + C_z + O_z^2(\boldsymbol{q}). \tag{6}$$

A plane passing through the origin point $\boldsymbol{q} = 0$ arises from $d_y(\boldsymbol{q}) = 0$ without considering $O_y^1(\boldsymbol{q})$. Similar to nodal rings protected by mirror symmetries, a nodal ring appears when $d_z(\boldsymbol{q}) = 0$ gives an enclosed three-dimensional manifold. Actually, the shape of the solution space is mainly determined by the low-order terms, whereas $O_y^1(\boldsymbol{q})$ just slightly affects the shape of the nodal ring. Generally, the nodal ring will be twisted and then it is no longer constrained in a plane.

As an example of materials realization, this type of nodal rings can also be found in the monoclinic AgO mentioned in Sec. III A. As shown in Fig. 4(a), there is only one crossing point because the nodal ring just intersects with high-symmetry lines at one point (or two equivalent points). It is worth mentioning that there are three nodal rings protected by inversion and time-reversal symmetries in the Brillouin zone shown in Fig. 4(b), but we only focus on the one with the center at the Γ point. This nodal ring is consistent with our above derivation and also satisfies other symmetries in its space group, such as a mirror symmetry about the $q_x = 0$ plane. Similarly, the Berry phase of this nodal ring is also π, and as drawn in Fig. 4(c), there are clear drumheadlike

phonon surface states between two bulk linear crossings along the $\tilde{Y}$-$\tilde{\Gamma}$-$\tilde{A}$ direction. This projected path centered around the $\tilde{\Gamma}$ point on the (010) surface is shown in Fig. 2(b) in detail. Meanwhile, in Fig. 4(d), the isofrequency surface depicted at the frequency of 10.76 THz reveals the shape of the nodal ring projected on the (010) surface and visible arc states. Similar to the (100) surface, the absence of trivial bulk states on the (010) surface is beneficial to experimental measurements.

C. Hybrid nodal rings protected by mirror, inversion, and time-reversal symmetries

In this section, we analyze the third type of nodal ring phonons protected by the combination of mirror, inversion, and time-reversal symmetries, i.e., hybrid nodal rings. In such cases, twisted nodal rings and in-plane nodal rings coexist around the time-reversal invariant momenta, forming crossed nodal rings with intersections along high-symmetry lines. Since mirror, inversion, and time-reversal symmetries are all taken into account, we need to combine two parts of the above derivation, which are

$$\begin{aligned} d_y(\boldsymbol{q}) &= C_y^z q_z + O_y^1(\boldsymbol{q}), \\ d_z(\boldsymbol{q}) &= \sum_{i=x,y,z} C_z^{ii} q_i^2 + C_z^{xy} q_x q_y + C_z + O_z^2(\boldsymbol{q}). \end{aligned} \tag{7}$$

$d_y(\boldsymbol{q})$ is still an odd function about q_z, but it is different from the first case. $d_y(\boldsymbol{q}) = 0$ may have solutions other than $q_z = 0$ that makes $d_i(\boldsymbol{q}) = 0$, leading to the formation of hybrid nodal rings.

Using first-principles calculations, we propose that the hybrid nodal rings can be realized in another phase of AgO [31]. In Fig. 5(a), we show the conventional cell of AgO, whose optimized lattice constants are $a = b = c = 6.797$ Å. This phase of AgO crystallizes in the tetragonal space group $I4_1/a$ (No. 88). In the conventional cell, Ag atoms occupy the $8c$ (0, 0, 0) and $8d$ (0, 0, 0.5) Wyckoff positions, while O atoms locate at the $16f$ (0.0885, 0.006 65, 0.207) Wyckoff positions. In Fig. 5(b), we depict the bulk Brillouin zone and its corresponding (001) surface Brillouin zone. Moreover, the calculated phonon spectrum is shown in Fig. 5(c), and the band crossings are marked in the green shadow. Figure 5(d) intuitively displays the nodal rings in the Brillouin zone, in which three intersecting nodal rings are drawn in different colors. To clearly show these three nodal rings, we project them on two planes A and B, as shown in Figs. 5(e) and 5(f), respectively. The projection of the blue nodal ring onto the A plane is a straight line, which means that it is a nodal ring protected by a mirror symmetry and constrained in the $q_z = 0$ plane. On the contrary, we can infer from the projections that the other two nodal rings are slightly twisted so they are protected by inversion and time-reversal symmetries.

We then give the theoretical proof of this hybrid nodal ring. The two crossing bands belong to the irreducible representations Γ_1^+ and Γ_2^-, respectively, so that the C_4 symmetry can be chosen as σ_z. Therefore, Eq. (7) can be simplified into

$$\begin{aligned} d_y(\boldsymbol{q}) &= C_y^{xx}\left(q_x^2 - q_y^2\right) q_z + C_y^{xyz} q_x q_y q_z + O_y^3(\boldsymbol{q}), \\ d_z(\boldsymbol{q}) &= C_z^{xx}\left(q_x^2 + q_y^2\right) + C_z^{zz} q_z^2 + C_z + O_z^2(\boldsymbol{q}). \end{aligned} \tag{8}$$

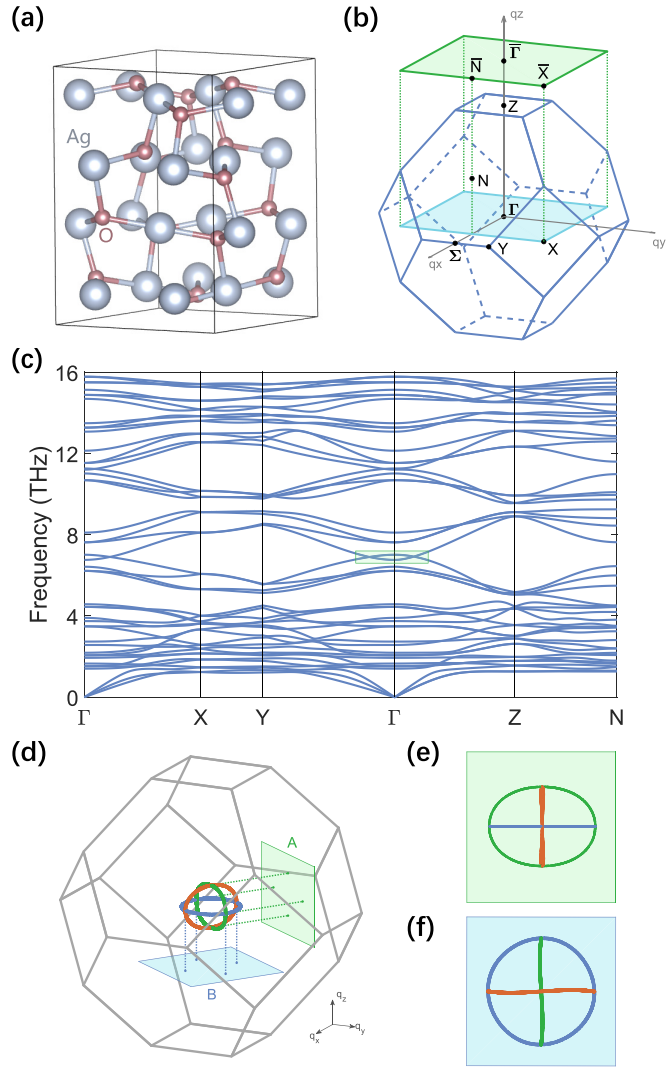

FIG. 5. (a) Crystal structure of AgO with space group $I4_1/a$. (b) Bulk Brillouin zone and projected Brillouin zone of the (001) surface. (c) Calculated phonon spectrum of this phase of AgO. (d) Nodal rings in the Brillouin zone. (e), (f) Projections of nodal rings on the A and B surfaces.

We first discuss the results without considering the higher-order terms. When $(C_y^{xyz})^2 + 4(C_y^{xx})^2 > 0$, we can get three mutually perpendicular intersecting planes from $d_y(\boldsymbol{q}) = 0$. Similarly, if $C_z C_z^{xx} < 0$ and $C_z C_z^{zz} < 0$, $d_z(\boldsymbol{q}) = 0$ gives an ellipse centered on Γ, so they intersect into three nodal rings perpendicular to each other. However, the existence of higher-order terms will affect the shape of the rings, that is, $O_y^2(\boldsymbol{q})$ in $d_z(\boldsymbol{q})$ slightly changes the form of the ellipse, but the intersecting rings are still in the three planes. Unlike $O_y^2(\boldsymbol{q})$, $O_y^3(\boldsymbol{q})$ in $d_y(\boldsymbol{q})$ releases the nodal rings from the planes. For example, $O_y^3(\boldsymbol{q})$ can be chosen as

$$O_y^3(\boldsymbol{q}) = \left(q_x^2 + q_y^2\right)\left[C_y^{xx\prime}\left(q_x^2 - q_y^2\right) q_z + C_y^{xyz\prime} q_x q_y q_z\right], \tag{9}$$

in which the latter part of this term has exactly the same form as the lower-order term of $d_y(\boldsymbol{q})$. It can be proved that this term satisfies the invariant theory and slightly bends the two nodal rings perpendicular to the $q_z = 0$. As a result, the

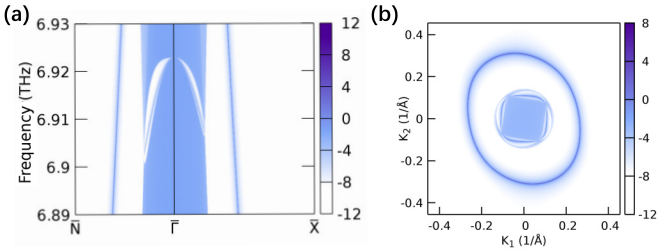

FIG. 6. (a) The phonon surface states along the $\bar{N}$-$\bar{\Gamma}$-$\bar{X}$ direction of the (100) surface. (b) The phonon surface Fermi arcs on the (001) surface Brillouin zone.

condition $d_y(\boldsymbol{q}) = d_z(\boldsymbol{q}) = 0$ gives three intersecting nodal rings, of which one lies in the $q_z = 0$ plane and the other two are twisted.

The calculated Berry phase is π and the surface states projected on the (001) surface along the $\bar{N}$-$\bar{\Gamma}$-$\bar{X}$ direction are shown in Fig. 6(a). The isofrequency surface at the frequency of 6.914 THz is shown in Fig. 6(b). Different from the single nodal ring in the monoclinic phase of AgO, the complex nodal rings make the surface states more prone to be covered. For example, we cannot see anything else except the bulk states around the $\bar{\Gamma}$ point. Although the area without bulk states is quite narrow, the nontrivial surface states are still observable (see Fig. 6).

IV. CONCLUSIONS

In summary, we systematically discuss the symmetry-protected nodal ring phonons by first-principles calculations and model analysis. At first, we propose that nodal ring phonons can be divided into three types: mirror symmetry protected, inversion and time-reversal symmetries protected, and hybrid. We also employ high-throughput calculations to find several candidate materials with the corresponding features in each case. Furthermore, we prove the existence of nodal ring phonons, which increases the reliability of our results. Moreover, the visible nontrivial surface states and isofrequency arc states are beneficial to various experimental measurements such as inelastic neutron scattering, inelastic x-ray scattering, and He atom scattering.

ACKNOWLEDGMENTS

This work is supported by the Guangdong Natural Science Funds for Distinguished Young Scholars (Grant No. 2017B030306008), the National Natural Science Foundation of China (NSFC, Grant No. 11974160), the fund of the Guangdong Provincial Key Laboratory of Computational Science and Material Design (Grant No. 2019B030301001), the Science, Technology and Innovation Commission of Shenzhen Municipality (Grants No. RCYX20200714114523069 and No. ZDSYS20190902092905285), and the Center for Computational Science and Engineering at Southern University of Science and Technology.

[1] N. P. Armitage, E. J. Mele, and A. Vishwanath, Rev. Mod. Phys. **90**, 015001 (2018).
[2] A. A. Burkov, M. D. Hook, and L. Balents, Phys. Rev. B **84**, 235126 (2011).
[3] H. Weng, C. Fang, Z. Fang, B. A. Bernevig, and X. Dai, Phys. Rev. X **5**, 011029 (2015).
[4] S. Borisenko, Q. Gibson, D. Evtushinsky, V. Zabolotnyy, B. Buchner, and R. J. Cava, Phys. Rev. Lett. **113**, 027603 (2014).
[5] M. Neupane, S.-Y. Xu, R. Sankar, N. Alidoust, G. Bian, C. Liu, I. Belopolski, T.-R. Chang, H.-T. Jeng, H. Lin *et al.*, Nat. Commun. **5**, 3786 (2014).
[6] S. M. Young, S. Zaheer, J. C. Y. Teo, C. L. Kane, E. J. Mele, and A. M. Rappe, Phys. Rev. Lett. **108**, 140405 (2012).
[7] X. Wan, A. M. Turner, A. Vishwanath, and S. Y. Savrasov, Phys. Rev. B **83**, 205101 (2011).
[8] K.-Y. Yang, Y.-M. Lu, and Y. Ran, Phys. Rev. B **84**, 075129 (2011).
[9] G. Bian, T.-R. Chang, R. Sankar, S.-Y. Xu, H. Zheng, T. Neupert, C.-K. Chiu, S.-M. Huang, G. Chang, I. Belopolski *et al.*, Nat. Commun. **7**, 10556 (2016).
[10] M. Phillips and V. Aji, Phys. Rev. B **90**, 115111 (2014).
[11] Y. Kim, B. J. Wieder, C. L. Kane, and A. M. Rappe, Phys. Rev. Lett. **115**, 036806 (2015).
[12] R. Yu, H. Weng, Z. Fang, X. Dai, and X. Hu, Phys. Rev. Lett. **115**, 036807 (2015).
[13] H. Weng, Y. Liang, Q. Xu, R. Yu, Z. Fang, X. Dai, and Y. Kawazoe, Phys. Rev. B **92**, 045108 (2015).
[14] T. Bzdusek, Q. Wu, A. Ruegg, M. Sigrist, and A. A. Soluyanov, Nature (London) **538**, 75 (2016).
[15] Q. Yan, R. Liu, Z. Yan, B. Liu, H. Chen, Z. Wang, and L. Lu, Nat. Phys. **14**, 461 (2018).
[16] W. Chen, H.-Z. Lu, and J.-M. Hou, Phys. Rev. B **96**, 041102(R) (2017).
[17] Z. Yan, R. Bi, H. Shen, L. Lu, S.-C. Zhang, and Z. Wang, Phys. Rev. B **96**, 041103(R) (2017).
[18] G. Chang, S.-Y. Xu, X. Zhou, S.-M. Huang, B. Singh, B. Wang, I. Belopolski, J. Yin, S. Zhang, A. Bansil *et al.*, Phys. Rev. Lett. **119**, 156401 (2017).
[19] R. Wang, J. Z. Zhao, Y. J. Jin, Y. P. Du, Y. X. Zhao, H. Xu, and S. Y. Tong, Phys. Rev. B **97**, 241111(R) (2018).
[20] R. Wang, J. Z. Zhao, Y. J. Jin, W. P. Xu, L.-Y. Gan, X. Z. Wu, H. Xu, and S. Y. Tong, Phys. Rev. B **96**, 121104(R) (2017).
[21] H. Miao, T. T. Zhang, L. Wang, D. Meyers, A. H. Said, Y. L. Wang, Y. G. Shi, H. M. Weng, Z. Fang, and M. P. M. Dean, Phys. Rev. Lett. **121**, 035302 (2018).
[22] T. Zhang, Z. Song, A. Alexandradinata, H. Weng, C. Fang, L. Lu, and Z. Fang, Phys. Rev. Lett. **120**, 016401 (2018).
[23] J. Li, Q. Xie, J. Liu, R. Li, M. Liu, L. Wang, D. Li, Y. Li, and X.-Q. Chen, Phys. Rev. B **101**, 024301 (2020).
[24] A. Levine, Nuovo Cimento **26**, 190 (1962).
[25] Y. Liu, Y. Xu, and W. Duan, Nat. Sci. Rev. **5**, 314 (2017).
[26] B. Peng, Y. Hu, S. Murakami, T. Zhang, and B. Monserrat, Sci. Adv. **6**, eabd1618 (2020).
[27] X. Li, B. Fauqué, Z. Zhu, and K. Behnia, Phys. Rev. Lett. **124**, 105901 (2020).
[28] Y. J. Jin, Z. J. Chen, B. W. Xia, Y. J. Zhao, R. Wang, and H. Xu, Phys. Rev. B **98**, 220103(R) (2018).

[29] B. Zheng, B. Xia, R. Wang, Z. Chen, J. Zhao, Y. Zhao, and H. Xu, Phys. Rev. B **101**, 100303(R) (2020).
[30] A. Grzelak, J. Gawraczynski, T. Jaron, M. Somayazulu, M. Derzsi, V. Struzhkin, and W. Grochala, Inorg. Chem. **56**, 5804 (2017).
[31] K. Yvon, A. Bezinge, P. Tissot, and P. Fischer, J. Solid State Chem. **65**, 225 (1986).
[32] See Supplemental Material at http://link.aps.org/supplemental/10.1103/PhysRevMaterials.5.084202 for more candidate materials, which includes Refs. [33,34].
[33] R. Van Essen and K. Buschow, J. Less-Common Met. **64**, 277 (1979).
[34] U. Flörke and W. Jeitschko, J. Less-Common Met. **86**, 247 (1982).
[35] G. Kresse and J. Furthmüller, Phys. Rev. B **54**, 11169 (1996).
[36] W. Kohn and L. J. Sham, Phys. Rev. **140**, A1133 (1965).
[37] J. P. Perdew, K. Burke, and M. Ernzerhof, Phys. Rev. Lett. **77**, 3865 (1996).
[38] G. Kresse and D. Joubert, Phys. Rev. B **59**, 1758 (1999).
[39] D. M. Ceperley and B. J. Alder, Phys. Rev. Lett. **45**, 566 (1980).
[40] A. Togo and I. Tanaka, Scr. Mater. **108**, 1 (2015).
[41] Q. Wu, S. Zhang, H.-F. Song, M. Troyer, and A. A. Soluyanov, Comput. Phys. Commun. **224**, 405 (2018).